


Meander pattern of spiral wave and the spatial distribution of its cycle lengthSergei F. Pravdin **Krasovskii Institute of Mathematics and Mechanics, 620108 Ekaterinburg, Russia
and Ural Federal University, High-Performance Computing Department, 620002 Ekaterinburg, Russia*Mikhail A. Patrakeeve *Krasovskii Institute of Mathematics and Mechanics, 620108 Ekaterinburg, Russia
and Ural Federal University, Mathematical Analysis Department, 620002 Ekaterinburg, Russia*Alexander V. Panfilov †*Ural Federal University, Research Laboratory “Mathematical Modeling in Physiology and Medicine Based on Supercomputers”,
620002 Ekaterinburg, Russia
and World-Class Research Center “Digital biodesign and personalized healthcare”, Sechenov University, 119146 Moscow, Russia*

(Received 9 November 2022; accepted 6 January 2023; published 26 January 2023)

One of the most interesting dynamics of rotating spiral waves in an excitable medium is meandering. The tip of a meandering spiral wave moves along a complex trajectory, which often takes the shape of an epitrochoid or hypotrochoid with inward or outward petals. The cycle lengths (CLs) of a meandering spiral wave are not constant; rather, they depend on the meandering dynamics. In this paper, we show that the CLs take two mean values, outside T^{out} and inside T^{in} the meandering trajectory with a ratio of $T^{\text{in}}/T^{\text{out}} = (n + 1)/n$ for the inward and $(n - 1)/n$ for the outward petals, where n is the number of petals in the tip trajectory. We illustrate this using four models of excitable media and prove this result. These formulas are shown to be suitable for a meandering spiral wave in an anatomical model of the heart. We also show that the effective periods of overdrive pacing of meandering spiral waves depend on the electrode location relative to the tip trajectory. Overall, our approach can be used to study the meandering pattern from the CL data; it should work for any type of dynamics that produces complex tip trajectories of the spiral wave, for example, for a drift due to heterogeneity.

DOI: [10.1103/PhysRevE.107.014215](https://doi.org/10.1103/PhysRevE.107.014215)**I. INTRODUCTION**

Spiral waves are a special class of rotating self-sustaining patterns in excitable media. They can be found in media of different nature, from various chemical reactions [1] to biological systems [2]. In the heart muscle, they underlie dangerous cardiac rhythm disturbances and usually have to be eliminated [3–5]. In the arrhythmia diagnostics and treatment, spiral wave cycle length (CL) and dynamics play an important role, as they can determine the type of arrhythmia [6,7].

There are several types of dynamics of spiral waves, the most important ones being stable rotation, meandering, drift, and breakup [8–10]. The tip of a stably rotating spiral wave revolves around a circular core, and the rotation has a constant period. A drift regime is the displacement of spiral waves in space usually due to heterogeneity.

Here, we study a type of dynamics called meandering [11,12], which is, in some sense, an intermediate type of dynamics between stable rotation and drift. The tip of a meandering spiral wave moves along a complex trajectory, which is often bounded. Meandering can occur in

homogeneous excitable media [13]. The meander dynamics is subdivided into subtypes such as quasiperiodic and chaotic meander based on the trajectory of a spiral wave tip [14]. The motion of a spiral wave affects its period, for example, due to the Doppler effect [15], so meandering also affects spiral wave CLs. CL varies in a quasiperiodic meander regime, and CL dispersion increases closer to the core [14]. However, to the best of our knowledge, there are no detailed studies on the spatial distribution of CL during meandering and its relation to the meandering patterns. Such study is interesting because the period of a spiral wave in the heart can be easily measured; thus, the relation between CL and meandering type can provide additional information on the dynamics of spiral waves. The generic aim of our paper is to study the relation between meandering patterns and spatial CL distribution for different types of meandering dynamics.

We reproduced all main types of meandering in the Barkley model [8,16], which is a classical model for meandering studies. We also performed simulations in FitzHugh-Nagumo models [17,18]. We showed that spatial period distribution qualitatively differs for two main meandering types: trajectories with inward or those with outward petals. For inward petals, the CL inside the trajectory is longer; for outward petals, CL is shorter inside than outside the trajectory. We proved this result analytically and derived a simple formula

*sfpravdin@imm.uran.ru; <http://sfpravdin.uran.ru/>†<https://heart.ugent.be>

that relates the number of petals in a trajectory and CL. This equation allows us to predict type of meandering trajectory from the measurements of a period. In addition, we studied meandering patterns in a three-dimensional (3D) anatomical model of the human heart and showed that the derived formula correctly predicted the meandering dynamics from CL measurement. Since an important way to remove spiral waves in the heart is pacing it with a period faster than the spiral wave period, we studied how CL distribution affects the process of spiral removal in a 2D domain and a 3D heart model. We tested how effective pacing periods are linked with meandering and CLs and found that the location of the pacing electrode plays an important role in the success of overdrive pacing.

II. METHODS

A. 2D simulations

Monodomain reaction-diffusion equations were used to simulate waves in isotropic tissue. For meandering spiral waves, we used a two-variable Barkley model of an excitable medium:

$$\frac{\partial u}{\partial t} = D\Delta u + \frac{1}{\epsilon}u(1-u)\left(u - \frac{v+b}{a}\right) - I_{\text{stim}}, \quad (1)$$

$$\frac{\partial v}{\partial t} = u - v, \quad (2)$$

where $u = u(\vec{r}, t)$ is the cell potential at point $\vec{r} = (x, y)$ at time t , D is the diffusion coefficient, $\Delta u = u_{xx} + u_{yy}$ is the Laplacian in plane (x, y) , $I_{\text{stim}}(\vec{r}, t)$ is the stimulation current, and ϵ, a, b are the model parameters. A tip trajectory with inward petals was obtained using Model 1, and a tip trajectory with outward petals was obtained using Model 2 (all their parameters are specified below in Table I).

For hypermeandering spiral waves, we utilized a two-variable FitzHugh-Nagumo (FHN) Model 3 with the following equations:

$$\frac{\partial u}{\partial t} = D\Delta u + \frac{1}{\epsilon}\left(u - \frac{u^3}{3} - v\right) - I_{\text{stim}}, \quad (3)$$

$$\frac{\partial v}{\partial t} = \epsilon(u + \beta - \gamma v), \quad (4)$$

where ϵ, β , and γ are the model parameters.

The spiral wave tip was found as a solution \vec{r}_{tip} of the system [19]

$$u(\vec{r}_{\text{tip}}, t) = u^*, \quad u(\vec{r}_{\text{tip}}, t + \Delta t) = u^*, \quad (5)$$

where u^* and Δt are model-specific parameters.

The sequential values of CL at a point $A(x, y)$ form a sequence CL_n . The CL at time t was computed as time between adjacent solutions $\tau_1 < t < \tau_2$ of equation $u(x, y, t) = u^*$ with a condition $\partial u/\partial t > 0$: $\text{CL}_n = \tau_2 - \tau_1$. The average CL in point A for a time segment $[\tau_i, \tau_j]$, denoted as $\langle T_{\text{sw}}^A \rangle$, was calculated as the mean value of the subsequence of CL_n :

$$\langle T_{\text{sw}}^A \rangle = \frac{\tau_j - \tau_i}{j - i}. \quad (6)$$

Pacing was implemented using the stimulation current I_{st} applied with a period T_{stim} using impulses with a duration t_{stim} from a moment τ_0 . This can be expressed using Iverson

TABLE I. Parameters of the 2D simulations with Models 1–4 (in dimensionless model units).

Parameter	Model 1	Model 2	Model 3	Model 4
Cell-level model parameters				
a	0.2661	0.73	$\epsilon = 0.08$	$a = 0.28$
b	-0.025	$b = 0.0475$	$\beta = 1.25$	$b = -0.025$
ϵ	0.02	$\epsilon = 0.0125$	$\gamma = 0.5$	$\epsilon = 0.02$
Tissue and domain parameters				
D	4	15	1	4
L	40	30	60	150
Numerical integration parameters				
dr	0.125	0.25	0.2	0.125
dt	0.0005	0.001	0.008	0.0005
S1S2 stimulation parameters				
t_{S2}	4.5	3.86	32	9
w_{S2}	0.55	0.3	0.5	0.3
u_{st}	1	1	2	1
u_0	0	0	-1.28	0
v_0	0	0	-0.57	0
Tip and CL search parameters				
Δt	0.1	0.1	1	0.05
u^*	0.5	0.5	0.5	0.5
Pacing parameters				
I_{st}	-5	-20	-10	-
t_{stim}	0.1	0.1	1	-
r_{stim}	2	2	1	-

brackets as

$$I_{\text{stim}}(x, y, t) = I_{\text{st}}[(x, y) \in \Omega_{\text{stim}}][t \geq \tau_0] \times \left[\left\{ \frac{t - \tau_0}{T_{\text{stim}}} \right\} \leq \frac{t_{\text{stim}}}{T_{\text{stim}}} \right], \quad (7)$$

where Ω_{stim} is the pacing area, a circle with a radius of r_{stim} , and the curly brackets denote the fractional part.

The domain was a square $L \times L$. The boundary condition was zero flux of potential u . The spiral waves were created using the S1S2 protocol; the area of the first stimulus ($u = u_{st}, v = v_0$) was $x < 10dr$; the second stimulus ($u = u_{st}$) was applied to area $y < w_{S2}L$ at time t_{S2} . The initial condition for other nodes was $u = u_0, v = v_0$. A numeric solution was obtained using an explicit Euler method.

Model 4 is a Barkley model used for 2D and 3D computations. The 2D simulation parameters of Models 1–4 are listed in Table I.

B. 3D simulations

A 3D heart model from [20] was used to examine our 2D findings in a more realistic case. We used a symmetric model of the human heart left ventricle (LV). We neglected the anisotropic nature of the myocardium and its mechanical deformations and used Barkley's isotropic electrical model [see Eqs. (1), (2)]. The shape of the 3D heart model is displayed in Fig. 1. A special curvilinear coordinate system (γ, ψ, φ) is linked with the LV model. Coordinate γ changes from γ_0 at the epicardium to γ_1 at the endocardium. Coordinate ψ , an analog of geographic latitude, is 0 at the base and $\psi = \pi/2$ at the apex. Finally, φ is a longitude changing from 0 to 2π .

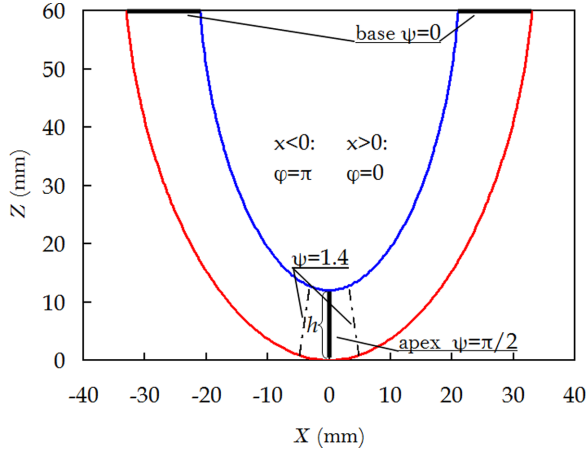


FIG. 1. Left ventricle model. Section by plane $y = 0$. Axes in mm. Red line, epicardium; blue line, endocardium; vertical black line, apical segment with $x = y = 0$, $\psi = \pi/2$, φ undefined, h is the apical thickness of the myocardial wall. Electrode 1 had $\psi > 1.4$; its borders are shown as dashed black lines. Two horizontal black lines, the base with $z = 60$ mm, $\psi = 0$.

The dynamics of a 3D spiral wave, also called a scroll wave, are characterized by the dynamics of its filament. The filament is an extension of the notion of the tip of a 2D spiral wave. A 2D spiral wave has a point tip at each moment of time, and a 3D scroll wave has a line of tip points, called a filament.

The scroll wave was created using the S1S2 protocol. Stimulated zones are specified in the Cartesian coordinate system in mm. First, nodes with coordinates $x \geq 0$, $0 \leq y \leq 5$, $50 \leq z$ were excited. Thus, S1 was applied to a small area at the LV base. Then, variable v at a control point $(0,0,5)$ was monitored; we performed the simulation until it exceeded $v_{\text{up}} = 0.2$ for the first time to ensure that the control point was depolarized. Then, we simulated until v reduced below $v_{\text{down}} = 0.05$ to ensure that the control point was repolarized. At that moment, we applied the second stimulation S2 at nodes with coordinates $y \geq 0$.

We scale Model 4 using data on the polymorphic ventricular tachycardia as an arrhythmia associated with spiral waves in the human heart. Its typical period is 224–270 ms [21]. We take the reference spiral wave period T_{sw} equal to 250 ms. Mean T_{sw} in the Model 4 is about 3.6 (see Sec. III E). So the model unit of time (MUT) T is 70 ms. The reference diffusion coefficient is $0.15 \text{ mm}^2/\text{ms}$ [22], and its model dimensionless value is taken equal $0.05 L^2/T$ [23] so the model unit of length (MUL) L is 14.4 mm. Based on that we provide dimensional data for the 2D and 3D simulations in Model 4 (see Table II).

The LV had thickness of 12 mm at the base and apex, cavity radius of 21 mm at the base, cavity depth of 48 mm, and shape factor of 0.85 (see details in Ref. [20]). Our numerical method of finding the Laplacian in the curvilinear coordinates and for the nonuniform LV grid was described in Ref. [24].

The reaction-diffusion system was integrated using the explicit Euler scheme. We chose the temporal step dt and the spatial step dr so that the stability criterion [25] $\dim D dt (dr)^{-2} \leq 1/2$, where \dim is the domain dimensionality, was satisfied for Models 1–4. Thus the explicit numerical method was stable.

TABLE II. Parameters of Model 4.

Parameter	Value
Cell-level parameters	
a	0.28
b	−0.025
ϵ	0.02
Scaling parameters	
Model T_{sw}	3.6 T
Reference T_{sw}	250 ms
MUT T	70 ms
MUL L	14.4 mm
Tissue and domain parameters	
D	$0.15 \text{ mm}^2/\text{ms}$
L in 2D	240 mm
Numerical integration parameters	
dr in 2D	0.5 mm
dr in 3D	1.6 mm
dt	0.035 ms
Pacing parameters	
t_{stim}	7 ms
I_{st}	−5
Tip and CL search parameters	
Δt	10.5 ms
u^*	0.5

C. Software

A high-performance cluster URAN (Krasovskii Institute of Mathematics and Mechanics, Ekaterinburg, Russia) was used for the computations. Software was written in C using OPENMP and ICC.

III. RESULTS

A. CL distribution and tip trajectories

Two main types of quasiperiodic meandering dynamics [14] are patterns where the tip of a spiral wave follows an epitrochoid trajectory (inward petals) or a hypotrochoid trajectory (outward petals) [26,27]. Let us consider them separately.

1. Inward petals

A spiral wave and its tip trajectory for the Model 1 are shown in Fig. 2(a). The curve has $n = 9$ inward petals and is nearly closed. The spiral wave rotates CW. We divided the entire domain into three concentric circular subdomains, a ring containing the flower trajectory, a disk located inside the ring, and an outside located exterior to the ring [Fig. 2(b)]. Let us consider two points, A , at the disk, and B , at the outside. Plots of transmembrane potential at these two points are visualized in Fig. 2(c). The CLs at the outside (blue) point are shorter than those at the inside point. The action potentials (APs) at these points almost coincide near $t = 49$ and $t = 84.5$ (these moments of time are shown as two dashed vertical lines). However, we observed ten blue and only nine red APs over that period. The time interval between the dashed vertical lines corresponds to the full rotation of the tip along the flower. We call it the full period of the tip rotation, which is approximately $T = 35.5$. The CLs at the blue and red points

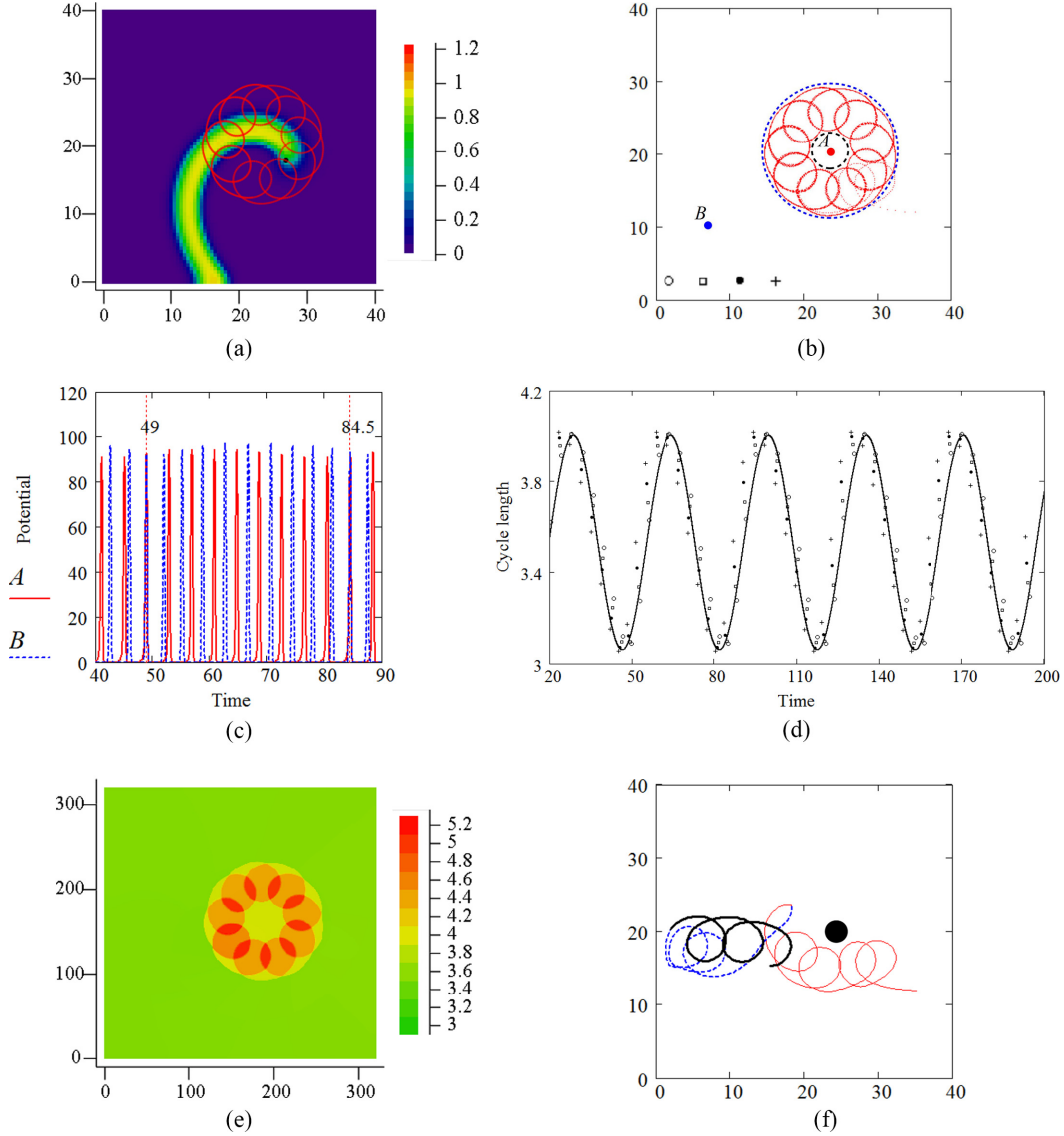


FIG. 2. Results for Model 1 with inward petals. (a) Spiral wave (state variable u), its tip (black dot), and tip trajectory (red curve). (b) Tip trajectory, points A , B , four detectors (circle, square, dot, and plus), and the subdomains. The disk is inside the black dashed circle; the ring is between the black and blue dashed circles; the outside is the remaining part of the domain. (c) Potential $100u$ for two points with coordinates $A(24, 20)$ (red, inside the curve) and $B(7, 10)$ (blue, outside the curve). Abscissa axis, time in model units. Vertical lines mark ends of a segment of time with 9 APs in point A and 10 APs in point B . The tip follows one full flower trajectory during that time segment. (d) Cycle lengths at the detectors outside the flower [see (b)]. (e) Average CLs in the entire domain (axes show indices of the nodes, not model units). (f) Tip trajectory with pacing (details in Sec. III D). (a), (b), (f) Axes in MULs.

are not constant and oscillate between 3.9 and 4.0 at point A and between 3.06 and 4.0 at point B . The average CLs are $T_A^{\text{in}} = 3.94$ and $T_B^{\text{out}} = 3.55$; they are in ratio 10:9 with an accuracy of 0.13%.

The CLs in different points at the outside are shown in Fig. 2(d). All CLs with a good accuracy belong to the same oscillating curve with a period of 35.5, maximum of approximately 3.99–4.01, minimum of 3.05–3.09, and average value of 3.55 regardless of the distance between the detector and the flower center. This curve can be reasonably well approximated by a sine function (shown by the brown line).

Figure 2(e) shows the spatial distribution of the average CLs at all nodes of the domain. We clearly see large regions where the CL equals $T_A^{\text{in}} = 3.94$ (yellow) and $T_B^{\text{out}} = 3.55$

(green) and longer periods in the ring (4–4.9, orange; 4.9–5.2, red). The longer CLs emerge because most of the points in any petal are temporarily inside the core while the tip follows the petal [see Fig. 2(a)]; thus, the wavefront cannot reach them.

Overall, the average CLs inside T^{in} and outside T^{out} the tip trajectory are in ratio

$$\frac{T^{\text{in}}}{T^{\text{out}}} = \frac{n+1}{n}, \tag{8}$$

where n is the number of petals.

2. Outward petals

The model with parameter set 2 has spiral wave and tip trajectory displayed in Fig. 3(a). The curve has five outward

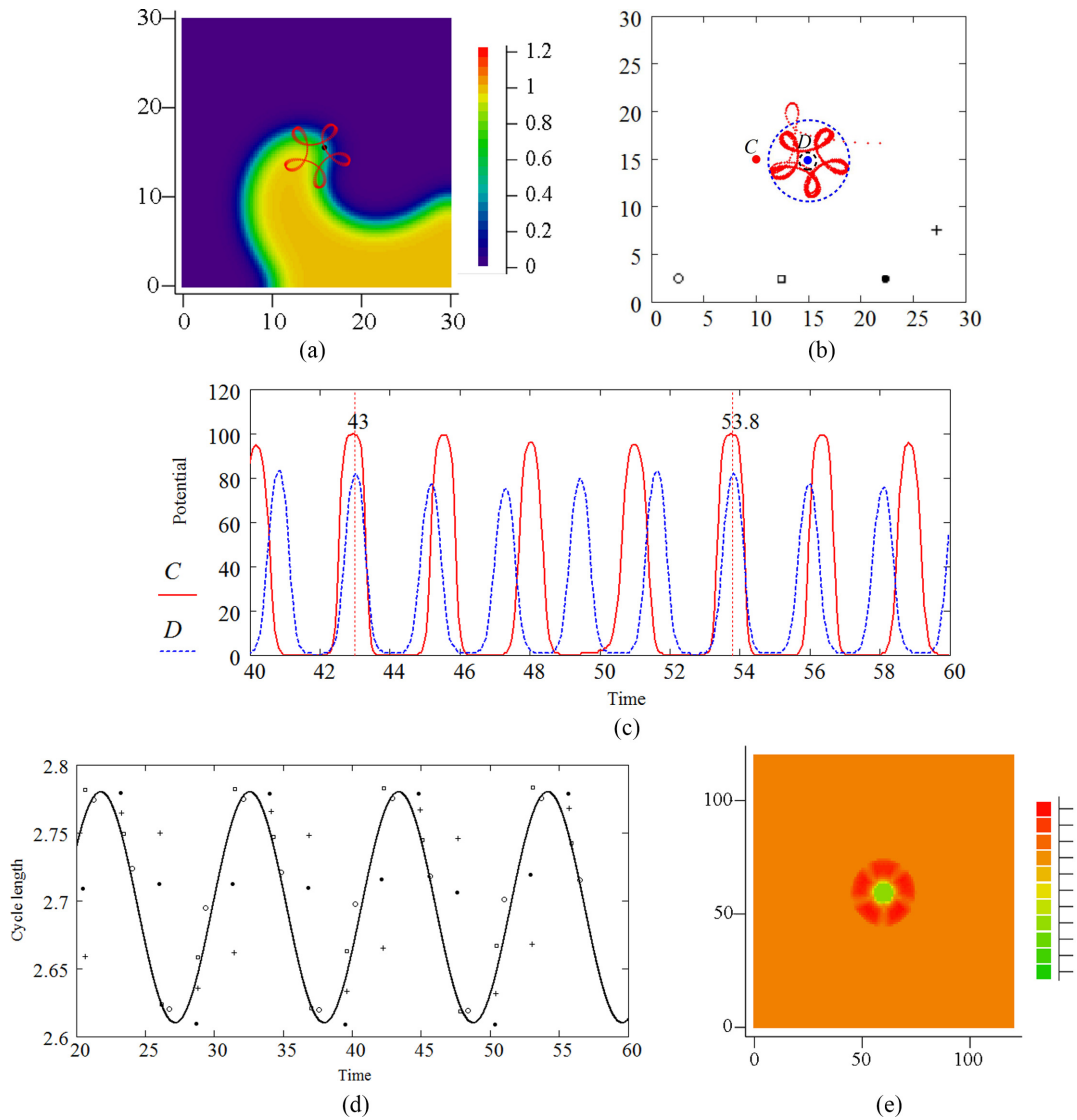


FIG. 3. Results for Model 2 with outward petals. (a) Spiral wave (state variable u), its tip (black dot), and tip trajectory (red curve). (b) Tip trajectory, points C , D , four detectors, and the subdomains. The disk is inside the black dashed circle; the ring is between the black and blue dashed circles; and the outside is the remaining part of the domain. (c) Potential $100u$ for two points with coordinates $C(10, 15)$ (red, outside the curve) and $D(15, 15)$ (blue, inside the curve). Abscissa axis, time in model units. Vertical lines mark ends of a segment of time with 4 APs in point C and 5 APs in point D . The tip drew one full flower during that time segment. (d) Cycle lengths at the detectors outside the flower [see (b)]. (e) Average CLs in the entire domain (axes show indices of the nodes, not model units). (a), (b) Axes in MULs.

petals and is nearly closed. The spiral wave rotates CW, and the tip follows its trajectory CCW. As in the previous case, three subdomains can be specified: the disk, inside the flower; the ring, which contains the tip flower, and the outside, the remaining part of the entire domain [see Fig. 3(b)]. Again, two points are chosen: C at the outside and D at the disk. A plot of potential in points C and D is visualized in Fig. 3(c). The CL is shorter in disk point D than in outside point C . The full period of the tip rotation along the flower is approximately $T = 10.8$. The potential develops four cycles in C and five cycles in D during the full period between the moments of time, shown as two dashed vertical lines. The CLs oscillate between 2.6 and 2.8 in point C and between 2.1 and 2.2 in point D . The average CLs are $T_D^{in} = 2.16$ and $T_C^{out} = 2.70$; they are in ratio 4:5.

The CLs in different points at the outside are shown in Fig. 3(d). All CLs with a good accuracy belong to the same oscillating curve with a period of 10.8, with a maximum of approximately 2.76–2.78, minimum of 2.61–2.63, and average value of 2.695, regardless of the distance between the detector and the flower center. The sine function (shown by brown line) approximates these points quite well.

Figure 3(e) shows the spatial distribution of the average CLs at all nodes of the domain. We clearly see large regions where the CL equals $T_D^{in} = 2.16$ (green) and $T_C^{out} = 2.70$ (orange) and longer periods at the ring (red). The CLs at the ring are longer because the meandering spiral wavefront cannot reach most of points in the ring when the tip is between two adjacent petals [see Fig. 3(a)].

Thus the ratio of average CLs inside T^{in} and outside T^{out} in the case of outward petals can be represented as

$$\frac{T^{\text{in}}}{T^{\text{out}}} = \frac{n-1}{n}, \quad (9)$$

where n is the number of petals. Now, let us consider the meandering from the viewpoint of geometric curve theory and explain the observed relations of CLs given by Eqs. (8), (9).

B. Curve theory

1. Closed tip curves

Notation used in the following consideration. For two rays $r_{1,2}$ having the same origin and continuously rotating with time $t \geq 0$, let us denote $\angle(r_1, r_2)$ the lifted angle from ray r_1 to ray r_2 , which is a continuous function, so that $\angle(r_1, r_2) \in [0, 2\pi)$ at $t = 0$. For a ray $r(t)$ that continuously changes with time t , let us denote $\angle r|_a^b$ the signed full rotation angle of r for $t \in [a, b]$ in the coordinate system moving parallel together with the ray origin.

Now, let us consider a domain with an excitable medium. The function $u(x, y, t)$ is a spiral-wave solution of the partial differential equations system, so the APs can be counted at any point of the domain using an appropriate potential level u^* . In the entire domain, for any moment of time, the level line $u(x, y) = u^*$ is a curve that consists of two parts, a wavefront, or forefront, where the potential is growing, and a waveback, or backfront, where it is falling. These two fronts meet at a point, wave tip, which can be numerically calculated using various algorithms, for example, by Fenton-Karma [19].

We will now focus on a meandering spiral wave with a smooth closed tip trajectory $\gamma(t)$, $t \geq 0$. The curve has a full period T , that is, $\gamma(0) = \gamma(T)$. The tip trajectory divides the plane into three parts, the disk, the ring, and the outside, as defined in Sec. III A 1.

At any point G of the tip trajectory, one can draw a wavefront, which is a curve that begins at point G (see Fig. 4). Thus, two tangents can be created, a tangent ray w to the tip trajectory γ toward the tip movement and a tangent ray s to the wavefront. Let angle $\psi = \angle(w, s)$. Traditionally, this angle can be from zero to $\pi/2$ for a rigidly rotating spiral wave according to the definition of core boundary points (see, e.g., definitions of the core based on points Q and q in Fig. 3 of Ref. [28]). Meandering spirals have this angle, generally, variable; however, the change is less than π during any period. Our literature search revealed that the question on the value of ψ has no clear answer. The angle ψ was drawn as zero in some papers, for example, Ref. [29], and not zero in others [14,30]. We will require $\psi(t)$ be a continuous function and

$$\psi(0) = \psi(T). \quad (10)$$

We recall that the CL of the spiral wave at a given point is the time between two successive wavefront arrivals to this point.

For a point B at the disk or outside, let us denote \mathcal{N}_B the number of APs at B —that is, the number of times the wavefront passes through B —during the full period T of the spiral wave. Without loss of generality, we can consider that point B is on the wavefront at time $t = 0$. We will show that \mathcal{N} is a constant \mathcal{N}_{in} at the entire disk and is another constant \mathcal{N}_{out} at the entire outside.

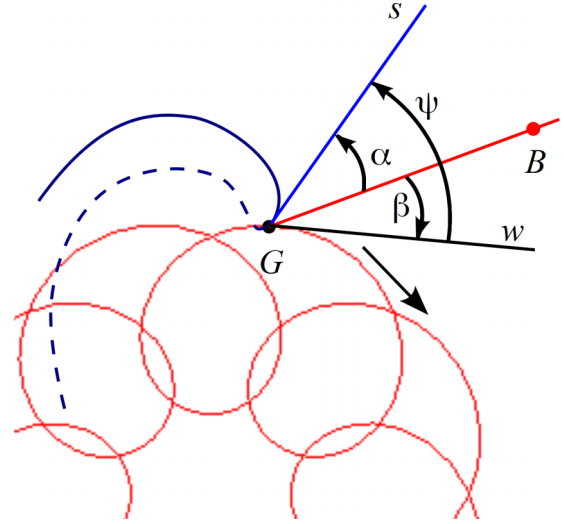


FIG. 4. Schematic of spiral wave forefront (blue solid curve), backfront (blue dashed curve), and tip trajectory fragment (red solid curve). G , a tip at an arbitrary time; B , a point at the disk or outside; s (blue straight line), the ray tangent to the forefront; w (black straight line), the ray tangent to the tip trajectory. The arrow shows the direction of tip motion.

Winding number \mathcal{W}_B of a point B not lying on the curve is the number of turns the vector $\vec{BG}(t)$ makes for $t \in [0, T]$, where $G = G(t)$ is a point on the curve (Fig. 4).

$\mathcal{W}_E = 0$ for any point E at the exterior part of the plane (i.e., the unbounded connectivity component of the complement of the curve). Winding number is an integer, and changing the curve orientation changes its sign. Let us consider CCW rotation as positive and CW rotation as negative.

Turning number \mathcal{T} of a smooth closed plane curve $\gamma(t)$ is the signed number of turns that the tangent vector to the curve makes for the full period. Strict mathematical definitions for the winding and turning number can be found in Ref. [31] for example.

Statement. For an arbitrary point B at the disk or outside, and for the full period,

$$\mathcal{N}_B = |\mathcal{W}_B - \mathcal{T}|. \quad (11)$$

Proof. Figure 4 displays a sketch of the spiral wavefront, tip trajectory, rays, and angles we use in the proof. We refer to angles $\alpha = \angle(GB, s)$, $\beta = \angle(GB, w)$, and $\psi = \angle(w, s)$.

The wavefront rotates in one direction only. Thus, after a transition through point B , the wavefront may go through it again only if the wavefront makes a full (or almost full) rotation. As the entire picture repeats after the full period, the absolute value of the change of α for $t \in [0, T]$ is the number of times the wavefront goes through B times 2π :

$$|\alpha(T) - \alpha(0)| = 2\pi\mathcal{N}_B.$$

We can write

$$\begin{aligned} \alpha(t) &= \angle(GB, s) = \angle(GB, w) + \angle(w, s) + 2\pi k(t) \\ &= \beta(t) + \psi(t) + 2\pi k(t) \end{aligned}$$

for an integer function $k(t)$. Functions $\alpha(t)$, $\beta(t)$, and $\psi(t)$ are continuous; thus, k is a continuous integer function and hence

TABLE III. Winding and turning numbers for flowerlike curves.

Petals	SW		Tip curve				
	rotation	Tip curve rotation	\mathcal{W}_{out}	\mathcal{W}_{in}	\mathcal{T}	\mathcal{N}_{out}	\mathcal{N}_{in}
inward	CW	CW	0	-1	$-n-1$	$n+1$	n
inward	CCW	CCW	0	+1	$n+1$	$n+1$	n
outward	CW	CCW	0	+1	$-n+1$	$n-1$	n
outward	CCW	CW	0	-1	$n-1$	$n-1$	n

a constant. The change in $\psi(t)$ during T is zero (10). Thus, the change in α during the full period T equals the change in β during T :

$$\alpha(T) - \alpha(0) = \beta(T) - \beta(0).$$

Note that the latter equals $\angle GB|_0^T - \angle w|_0^T$. The full rotation angle of GB is the winding number times 2π , and that of w is the turning number times 2π :

$$\alpha(T) - \alpha(0) = 2\pi(\mathcal{W}_B - \mathcal{T}).$$

Finally,

$$\mathcal{N}_B = |\mathcal{W}_B - \mathcal{T}|.$$

Table III summarizes the winding and turning numbers for the flowers with n outward and inward petals. The formal rules for computing the numbers for arbitrary curves can be found, for example, in Refs. [31,32]. As $T = \mathcal{N}_B(T_{\text{sw}}^B)$ for any point B at the disk or outside, the fraction $T^{\text{in}}/T^{\text{out}}$ equals $\mathcal{N}_{\text{out}}/\mathcal{N}_{\text{in}}$, which corroborates our Eqs. (8) and (9).

2. Nonclosed tip curves

If the tip curve is not closed and there is no distinct petal number, we can still define areas of outside, ring, and disk and generalize our results.

Outside is the exterior part of the plane (i.e., the unbounded connectivity component of the complement of the curve).

Center is the mean of the tips.

Disk is the maximal circle of the center that has no interior intersection with the tip curve, except maybe an initial segment of the curve.

Finally, ring is the complement of the outside and disk union.

For the case of nonclosed curves, Eq. (11) can be rewritten with winding and turning angles instead of numbers:

$$\mathcal{N}_B(t) \approx \left\lfloor \frac{|\angle \mathcal{W}_B(t) - \angle \mathcal{T}(t)|}{2\pi} \right\rfloor, \quad (12)$$

where \mathcal{N}_B is the integer number of action potentials in the point for time from 0 to t , $\angle \mathcal{W}_B$ is the winding angle following $\angle \mathcal{W}_B(0) = 0$, $\angle \mathcal{T}$ is the turning angle following $\angle \mathcal{T}(0) = 0$, and $\lfloor \dots \rfloor$ denotes the floor function. This formula is valid only approximately because the length GB changes with every action potential.

A nonclosed tip curve shows no distinct number of petals n , so the use of the results from Table III requires a new, more general definition for n . First, n is the number of rotations the

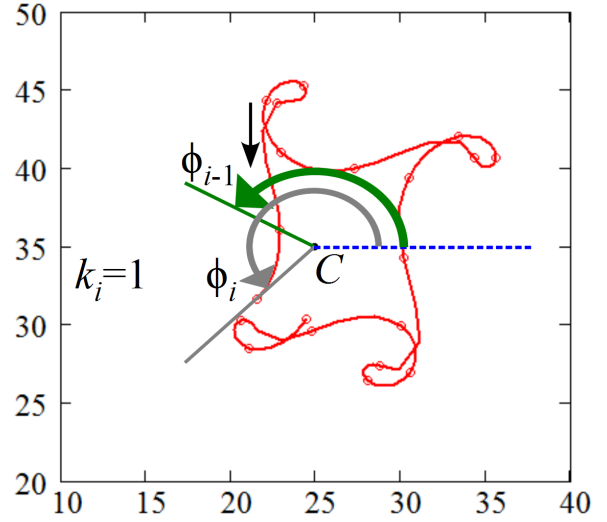


FIG. 5. Schematic of discrete full angle ϕ . C , arbitrary disk point; blue dashed line, arbitrary axis; red curve, tip trajectory; red circles, discrete tip positions (for clarity, every fifth tip is drawn); black arrow displays the direction of tip motion near the $(i-1)$ th tip. Green arrow and line show the lifted angle ϕ_{i-1} for the $(i-1)$ th tip, and gray arrow and line show ϕ_i for the i th tip. Note that $k_i = 1$ here to neutralize the discontinuity of atan2 .

spiral undergoes per turnover of the tip around the disk:

$$n = \frac{1}{\omega T^{\text{in}}}, \quad (13)$$

where ω is the angular speed of the tip rotation around the disk; note that T^{in} is the average CL at the disk. Second, consider a lifted angle ϕ of tip position relative to an arbitrary ray that begins in a point at the disk (Fig. 5). Then, the tip angular speed ω (in turnovers per time unit) can be estimated using the limit of lifted angle ϕ per time:

$$\omega = \lim_{t \rightarrow \infty} \frac{\phi(t)}{2\pi t} = \lim_{n \rightarrow \infty} \frac{\phi_n}{2\pi t_n}, \quad (14)$$

where discrete angles ϕ_n are computed for times t_n and can be found using a recurrent formula

$$\phi_i = \phi_{i-1} + \Delta\phi_i, \quad (15)$$

$$\Delta\phi_i = \text{atan2}(y_i - y_c, x_i - x_c) - \text{atan2}(y_{i-1} - y_c, x_{i-1} - x_c) + 2\pi k_i, \quad (16)$$

where (x_c, y_c) are the coordinates of the disk point, (x_i, y_i) are the coordinates of the i th tip, and the integer k_i is chosen such that $|\Delta\phi_i| < \pi$.

If a nonclosed trajectory is approximately closed after p tip rotations around the flower center and q petals, which take time t , we can estimate the angular rotation speed $\omega = p/t$ and average CL at the disk $T^{\text{in}} = t/q$, so $n = q/p$. Computing the winding and turning numbers for all four configurations, as shown in Table III, we find $T^{\text{in}}/T^{\text{out}} = \mathcal{N}_{\text{out}}/\mathcal{N}_{\text{in}} = (q+p)/q = (n+1)/n$ for inward petals and $|q-p|/q = (n-1)/n$ for outward petals. Thus, Eqs. (8) and (9) can be still applicable for nonclosed tip curves. In the following sections, we will test the accuracy of those equations.

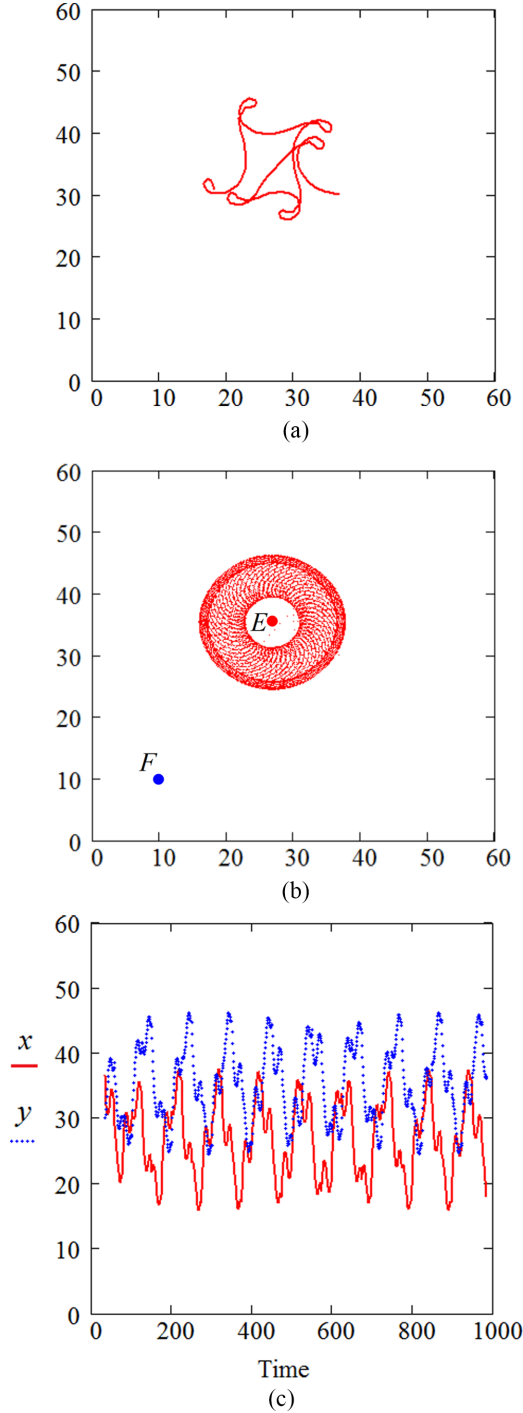


FIG. 6. Results for a hypermeandering spiral wave, FHN model 3. (a) Tip curve for 180 T. (b) Tip points (not connected) for 10^4 T. The disk, ring, and outside are clearly observable. (c) Tip coordinates x, y vs. time. Axes in all plots in model units.

C. Hypermeander

For this regime, we use the FHN model 3 and obtain a tip trajectory shown in Figs. 6(a), 6(b). Winfree proposed [10] to define hypermeander as spiral tip dynamics in which “tip paths could not be described in terms of two periods;” that is, the coordinates as functions of time are not just sums of two sinusoids and a linear function. We validate if such a property

is fulfilled in the considered case [see Fig. 6(c) for the tip coordinate plots].

The CLs are measured in two points, $E = (27, 36)$ inside the curve and $F = (10, 10)$ outside the curve.

Point	Cycle lengths			T_{max}
	min	max	mean	
E	24.1	25.7	24.9	32.0
F	29.3	35.5	32.4	32.6

Model 3 shows $\omega = 9.4 \times 10^{-3}$ turnovers per MUT, $T^{in} = 24.9$ and thus $n = 4.3$ petals per tip turnover around point E . Furthermore, as the petals are outward, the CL ratio has to be [see (9)]

$$\frac{n - 1}{n} = \frac{3.3}{4.3} = 0.767,$$

which is close to

$$\frac{T^{in}}{T^{out}} = \frac{24.9}{32.4} = 0.769$$

with an accuracy of 0.15%.

D. Overdrive pacing

Previously, we performed extensive studies on the possibility to supersede a spiral wave by applying external stimulation with a high frequency (overdrive pacing) [23,33–39]. These studies indicated that the maximum effective period of overdrive pacing T_{max} is less than T_{sw} for stably rotating spirals. However, CLs of meandering spirals vary in space and time, and we cannot refer to T_{sw} as a single distinct value. CL can be characterized by its minimal, maximal, and average $\langle T_{sw} \rangle$ values. To study the relation between these values and effective pacing periods, we simulated spiral waves and overdrive pacing using electrodes located at points A, B for inward-petal meandering (see Fig. 2) and points C, D for outward-petal meandering (see Fig. 3). We paced for 1000 MUT, which is approximately 300–400 rotation cycles. The computed values of T_{max} are shown in Table IV.

We expect that $T_{max} \approx \langle T_{sw} \rangle$ generally. However, at point A , T_{max}^A is substantially less than $\langle T_{sw}^A \rangle$. This is because pacing with the period close to $\langle T_{sw}^A \rangle$ breaks the closed curve of the tip trajectory, so that the pacing electrode is not inside the curve anymore. Thus, the electrode has to be paced faster. An example of the tip trajectory during ineffective pacing with a period of 3.7 is shown in Fig. 2(f). The electrode is

TABLE IV. Cycle lengths and maximal pacing periods.

Point	Petals in/out	Point in/out the tip curve	Cycle lengths			Pacing
			min	max	mean $\langle T_{sw} \rangle$	period T_{max}
A	inward	inside	3.9	4.0	3.94	3.6775
B	inward	outside	3.06	4.0	3.55	3.544
C	outward	outside	2.6	2.8	2.70	2.699
D	outward	inside	2.1	2.2	2.16	–

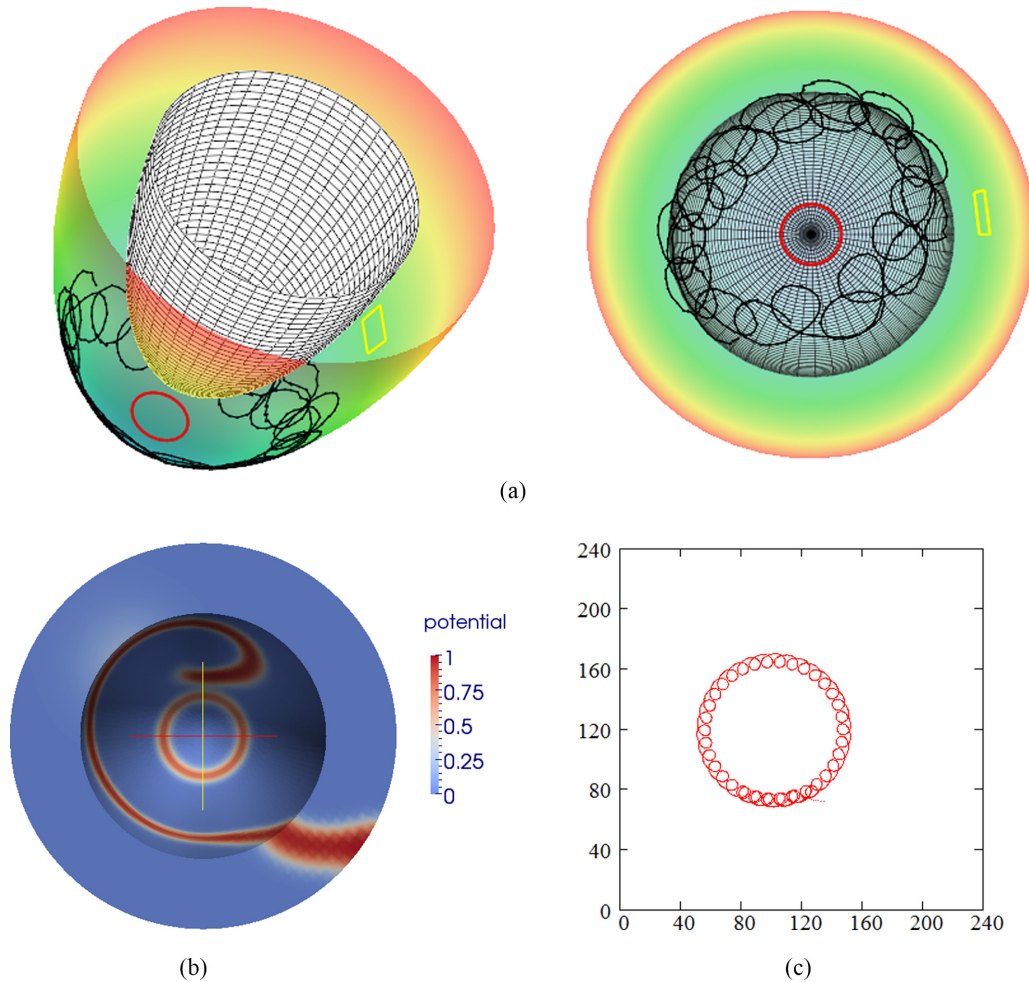


FIG. 7. Simulation results with Model 4 in the LV model and in two dimensions. (a) The LV model, epicardium (semitransparent colored surface, the color denotes z coordinate), endocardium (meshed surface, opaque in the left panel, semitransparent in the right panel), tip trajectory on the epicardium (for time 700–7000 ms, black curve), electrode 1 border on the epicardium (red curve), and electrode 2 border on the epicardium (yellow curve). Side and up view (left panel); bottom view (right panel). (b) Scroll wave shown on the model surface, up view. X axis (red); Y axis (yellow); color denotes potential u . The circular wave is emerged by electrode 1. Pacing period of 189 ms. (c) Tip trajectory in two dimensions. Axes in mm.

shown as a black circle and is located inside the flower, at the disk. The first part of the curve is red (thin line; time from 4.6, when the tip appeared first, to 20.6, when the pacing changed the tip dynamics); it is a fragment of the typical nine-petal flower curve. The second part of the curve is blue (dashed line; time from 20.6 to 30.1, when the tip repelled from the border); it is caused by the pacing. The third part is black (time 30.1–39.6); it is close to a shifted nine-petal flower. Note that the electrode is not at the disk anymore but at the new flower's outside, where the average CL of the spiral wave is shorter. The theory of overdrive pacing works perfectly for point B , where $T_{\max}^B \approx \langle T_{\text{sw}}^B \rangle$. The same is true for point C .

Finally, point D is located inside the outward-petal curve. In this area, CLs are especially short, and the electrode cannot assimilate pacing faster than that at which the spiral wave excites it. Thus, no effective pacing periods are found for stimulation at point D .

E. Simulations in the cardiac LV model

We use Model 4 for 3D simulations (Fig. 7). As a preliminary step, we study its 2D properties in the spiral-wave regime first. The 2D spiral wave shows a typical meandering pattern with tip trajectory of $n_2 = 34$ inward petals [see Fig. 7(c)]. Its CLs oscillate between 207 ms and 291 ms outside the tip curve (with an average of 3.6, or $T_{2D}^{\text{out}} = 249$ ms) and between 252 ms and 267 ms inside it (with an average of $T_{2D}^{\text{in}} = 260$ ms) (see Fig. 8, left panel). Equation (8) provides the average CLs ($T_{2D}^{\text{in}}/T_{2D}^{\text{out}} = (n_2 + 1)/n_2$) with an accuracy of 1.3%.

The dynamics of the 3D scroll wave without pacing include two phases. First, the wave core located between the apex and the base and rotated approximately three times about the LV vertical axis. The path has special coordinate $\psi \approx 1$ [the first-phase epicardial tip trajectory for time 700–7000 ms is shown in Fig. 7(a) as a black curve]. During the first drift phase, the spiral makes approximately $n_3 = 26$ rotations about its core

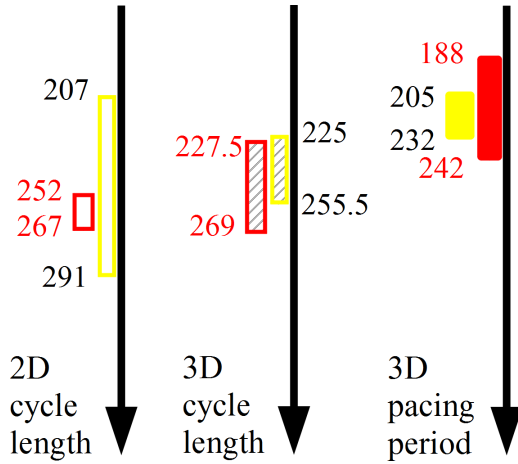


FIG. 8. A schematic comparison of CLs and pacing periods, ms, for Model 4. CLs for the 2D spiral wave (empty bars on the left), for the 3D scroll wave in the LV model (hatched bars in the middle), and pacing periods for the 3D LV scroll wave (filled bars on the right). Red, a node inside the tip curve and electrode 1 [red in Fig. 7(a)], which is also located inside the curve. Yellow, a node outside the tip curve and electrode 2 [yellow in Fig. 7(a)] also located outside the curve.

per rotation about the LV axis. Then, the core drifts toward the base, the rotation about the LV axis slows down, and finally, the core stays near the base. CLs oscillate in three dimensions, as in the 2D case, but minimal and maximal 3D CLs differ from their 2D values (compare left and middle bars in Fig. 8).

Equation (8) can also be used to estimate the number n_3 of 3D petals based on the average CLs:

$$n \approx \left(\frac{T^{\text{in}}}{T^{\text{out}}} - 1 \right)^{-1},$$

so the estimated number of petals is $n_3 \approx 31$. Thus, our approach estimates the number of petals (31 vs. 26) reasonably well.

We measured the minimal and maximal effective pacing periods from two electrodes. Electrode 1 is located at the apex, and electrode 2 has coordinate $\psi \approx 0.6$ between the core drift trajectory and the base [Fig. 7(b)]. Pacing from apical electrode 1 is effective if its period is between 188 ms and 242 ms (Fig. 8, see the red bar in the right panel), and pacing from electrode 2 is effective if its period is between 205 ms and 232 ms (the yellow bar in the right panel).

The range of 2D spiral wave CLs is wider at the point outside the tip curve than inside it, and the average CLs are quite close, 249 ms vs. 260 ms. We expect the maximal effective pacing periods to be in the same relation, $T_{\text{max}}^{\text{out}} < T_{\text{max}}^{\text{in}}$. This was actually the case because we obtained $T_{\text{max}}^{\text{out}} = 232 \text{ ms} < T_{\text{max}}^{\text{in}} = 242 \text{ ms}$. The average 3D CLs are in relation (8) with an accuracy of 0.6%.

The mean 3D CLs are 248 ms inside the tip curve and 240 ms outside it; the difference is 8 ms, which is about 3%. In practice, a flowerlike scroll wave tip trajectory with petals toward the apex means that the electrode should be placed at the apex.

IV. DISCUSSION AND CONCLUSIONS

In this study, we perform a comprehensive analysis of CL distribution in case of meandering spiral waves. The distribution has two main spatial areas: outside the meandering region and inside it. The average CLs in these regions depend on the type of the meandering pattern (outward or inward).

Winfree mentioned that excitation comes inside a flower's center three times when the spiral makes two rotations if the tip trajectory is a triangular flower [10]. The interval between the reexcitations inside the flower is proposed to be $T^{\text{in}} = (1 - \phi/2\pi)T_{\text{sw}}$ where ϕ is the angle between the successive vertices of the meander flower [10].

Barkley considered meandering spirals in the laboratory frame (stationary coordinates) and rotating frame [13,40]. The rotational velocity of the rotating frame is ω_1 , and the spiral wave frequency as seen in the rotating frame is ω_2 . The frequency ratio ω_2/ω_1 is 5/4 for “a closed five-lobed tip path” [40]. Spiral waves in heterogeneous media can show different periods inside and outside the area of increased action potential duration (APD) [41].

Here, we generalize these results and show analytically that the average CLs in the disk and outside areas follow Eqs. (8) and (9). These equations can also be used to determine the type of meandering pattern just from the measurement of average CL of excitation. A similar approach works in 3D anatomical models of the heart.

Use of dimensionless model units when describing dimensional objects may be unusual or misleading. However, obtaining dimensional scaling for generic two-variable models is nontrivial, and various research groups use different approaches. Time can be naturally scaled based on, for example, the APD, which can work well for some models. However, the Barkley model and FHN model were not specially designed for the cardiac tissue, in which the APD and refractory period are similar. In contrast, the APDs in these models are substantially shorter than their refractory periods. The reason is that the small parameter ϵ , which determines the model dynamics, is constant in these models. However, the refractory period (not the excited state duration) is the main determinant of the spiral wave period. This problem can be solved by making ϵ dependent on the transmembrane voltage. An example is the two-variable Aliev-Panfilov model [42] where the APD is close to the refractory period. However, we decided to use the Barkley and FHN models as they are classical models to study various meandering patterns.

This paper is focused on spiral wave dynamics so the most natural temporal scaling seems to be based not on the APD but on the spiral wave period. We scale the 3D LV model using data on the polymorphic ventricular tachycardia as it is widely believed that this arrhythmia is associated with spiral waves in the human heart. We also provide information on the dimensionless version of Model 4, which is used in 2D simulations.

We address the problem of removal of meandering spiral waves using overdrive pacing and search for possible reasons of its failure. Our earlier 2D simulations showed that the interval of effective pacing periods depends essentially on the model; it is usually wider in Aliev-Panfilov model [37,38] than in the ionic Luo-Rudy I (LR-I) model or ten

Tusscher-Panfilov 2006 model [33,36]. Too fast pacing can lead to dynamical instabilities and breakup [35]. At the same time, too slow pacing can be effective in 2D media but ineffective in a 3D slab if the scroll wave filament is unstable [39].

Our results can explain why overdrive pacing can lose its tip-shifting effect after several stimuli. That could happen if the tip trajectory has petals toward the pacing electrode. For example, a scroll wave can meander in the cardiac LV while revolving about the ventricle long axis and the apical electrode.

Another source of CL change in spiral waves is local heterogeneities. It is well-known that a local heterogeneity of a large enough size can anchor a spiral wave permanently. In addition, a spiral wave can be trapped temporarily [43] if the heterogeneity size is between certain limits. A possible direction of future research can be overdrive pacing of meandering spiral waves in heterogeneous media.

Hypermeander is a meander subtype that is more complex than a two-period tip motion. It is observed in several mod-

els, such as the Belousov-Zhabotinsky (BZ) medium model, Oregonator, Beeler-Reuter, and Noble [10] models. The first numerical demonstration of Winfree's hypermeander in a BZ model was in 1979 [44]. Our earlier simulations in the LR-I model involved hypermeander patterns [36], but the tip trajectory had no inner area. This paper shows that the methodology of Eqs. (8) and (9) works for the hypermeander case. The LR-I model can show a hypermeander with a clear hole inside the tip curve [14,45–47], so it would be interesting to apply the theory for some of the cited models.

ACKNOWLEDGMENTS

A.V.P.'s research at Sechenov University was financed by the Ministry of Science and Higher Education of the Russian Federation within the framework of state support for the creation and development of World-Class Research Centers "Digital biodesign and personalized healthcare" (Grant No. 075-15-2022-304).

-
- [1] R. Imbuhl and G. Ertl, Oscillatory kinetics in heterogeneous catalysis, *Chem. Rev.* **95**, 697 (1995).
 - [2] C. J. Weijer, Dictyostelium morphogenesis, *Curr. Opin. Genet. Dev.* **14**, 392 (2004).
 - [3] J. D. Fisher, R. Mehra, and S. Furman, Termination of ventricular tachycardia with bursts of rapid ventricular pacing, *Am. J. Cardiol.* **41**, 94 (1978).
 - [4] W. Grimm, E. Plachta, and B. Maisch, Antitachycardia pacing for spontaneous rapid ventricular tachycardia in patients with prophylactic cardioverter-defibrillator therapy, *Pacing Clin. Electrophys.* **29**, 759 (2006).
 - [5] J. I. Haft, B. D. Kosowsky, S. H. Lau, E. Stein, and A. N. Damato, Termination of atrial flutter by rapid electrical pacing of the atrium, *Am. J. Cardiol.* **20**, 239 (1967).
 - [6] A. Garfinkel, P. S. Chen, D. O. Walter, H. S. Karagueuzian, B. Kogan, S. J. Evans, M. Karpoukhin, C. Hwang, T. Uchida, M. Gotoh, O. Nwasokwa, P. Sager, and J. N. Weiss, Quasiperiodicity and chaos in cardiac fibrillation, *J. Clin. Invest.* **99**, 305 (1997).
 - [7] A. Garfinkel and Z. Qu, in *Nonlinear Dynamics of Excitation and Propagation in Cardiac Muscle*, 4th ed. (Saunders, Philadelphia, 2004), Chap. 36, pp. 327–335.
 - [8] D. Barkley, Euclidean Symmetry and the Dynamics of Rotating Spiral Waves, *Phys. Rev. Lett.* **72**, 164 (1994).
 - [9] A. T. Winfree, Spiral waves of chemical activity, *Science* **175**, 634 (1972).
 - [10] A. T. Winfree, Varieties of spiral wave behavior: An experimentalist's approach to the theory of excitable media, *Chaos: An Interdisciplinary J. Nonlinear Sci.* **1**, 303 (1991).
 - [11] V. S. Zykov, Cycloidal circulation of spiral waves in an excitable medium, *Biofizika* **31**, 862 (1986).
 - [12] V. S. Zykov, *Simulation of Wave Processes in Excitable Media* (Manchester University Press, Manchester, 1987).
 - [13] D. Barkley, Spiral meandering, in *Chemical Waves and Patterns* (Springer, Netherlands, 1995), pp. 163–189.
 - [14] Z. Qu, F. Xie, A. Garfinkel, and J. N. Weiss, Origins of spiral wave meander and breakup in a two-dimensional cardiac tissue model, *Ann. Biomed. Eng.* **28**, 755 (2000).
 - [15] S. F. Pravdin and A. V. Panfilov, Doppler shift during overdrive pacing of spiral waves. Prediction of the annihilation site, *Chaos, Solitons & Fractals* **155**, 111782 (2022).
 - [16] D. Barkley, A model for fast computer simulation of waves in excitable media, *Physica D* **49**, 61 (1991).
 - [17] R. FitzHugh, Impulses and physiological states in theoretical models of nerve membrane, *Biophys. J.* **1**, 445 (1961).
 - [18] J. Nagumo, S. Arimoto, and S. Yoshizawa, An active pulse transmission line simulating nerve axon, *Proc. IRE* **50**, 2061 (1962).
 - [19] F. Fenton and A. Karma, Vortex dynamics in three-dimensional continuous myocardium with fiber rotation: Filament instability and fibrillation, *Chaos* **8**, 20 (1998).
 - [20] S. F. Pravdin, V. I. Berdyshev, A. V. Panfilov, L. B. Katsnelson, O. Solovyova, and V. S. Markhasin, Mathematical model of the anatomy and fibre orientation field of the left ventricle of the heart, *Biomed. Eng. Online* **12**, 54 (2013).
 - [21] S. Viskin, E. Chorin, D. Viskin, A. Hochstadt, A. L. Schwartz, and R. Rosso, Polymorphic ventricular tachycardia: terminology, mechanism, diagnosis, and emergency therapy, *Circulation* **144**, 823 (2021).
 - [22] K. H. W. J. ten Tusscher and A. V. Panfilov, Alternans and spiral breakup in a human ventricular tissue model, *Am. J. Physiol.: Heart Circ. Physiol.* **291**, H1088 (2006).
 - [23] S. F. Pravdin, T. I. Epanchintsev, H. Dierckx, and A. V. Panfilov, Scroll wave with negative filament tension in a model of the left ventricle of the human heart and its overdrive pacing, *Phys. Rev. E* **104**, 034408(2021).
 - [24] S. F. Pravdin, H. Dierckx, L. B. Katsnelson, O. Solovyova, V. S. Markhasin, and A. V. Panfilov, Electrical wave propagation in an anisotropic model of the left ventricle based on analytical description of cardiac architecture, *PLoS ONE* **9**, e93617 (2014).
 - [25] A. C. Hindmarsh, P. M. Gresho, and D. F. Griffiths, The stability of explicit Euler time-integration for certain finite difference approximations of the multi-dimensional advection-diffusion equation, *Int. J. Numer. Meth. Fluids* **4**, 853 (1984).

- [26] E. W. Weisstein, Web page Epitrochoid. From MathWorld – A Wolfram Web Resource, <https://mathworld.wolfram.com/Epitrochoid.html>.
- [27] E. W. Weisstein, Web page Hypotrochoid. From MathWorld – A Wolfram Web Resource, <https://mathworld.wolfram.com/Hypotrochoid.html>.
- [28] O.-U. Kheowan, V. Gáspár, V. S. Zykov, and S. C. Müller, Measurements of kinematical parameters of spiral waves in media of low excitability, *Phys. Chem. Chem. Phys.* **3**, 4747 (2001).
- [29] V. Hakim and A. Karma, Theory of spiral wave dynamics in weakly excitable media: Asymptotic reduction to a kinematic model and applications, *Phys. Rev. E* **60**, 5073 (1999).
- [30] T.-C. Li, B.-W. Li, B. Zheng, H. Zhang, A. Panfilov, and H. Dierckx, A quantitative theory for phase-locking of meandering spiral waves in a rotating external field, *New J. Phys.* **21**, 043012 (2019).
- [31] M. Berger and B. Gostiaux, *Differential Geometry* (Springer, New York, 1988).
- [32] H. Whitney, On regular closed curves in the plane, *Compositio Mathematica* **4**, 276 (1937).
- [33] T. Epanchintsev, S. Pravdin, and A. Panfilov, Simulation of spiral wave superseding in the Luo–Rudy anisotropic model of cardiac tissue with circular-shaped fibres, *J. Comput. Sci.* **32**, 1 (2019).
- [34] S. F. Pravdin, T. I. Epanchintsev, T. V. Nezlobinskii, and A. V. Panfilov, Induced drift of scroll waves in the Aliev–Panfilov model and in an axisymmetric heart left ventricle, *Russ. J. Numer. Anal. Math. Mod.* **35**, 273 (2020).
- [35] S. F. Pravdin, T. I. Epanchintsev, and A. V. Panfilov, Overdrive pacing of spiral waves in a model of human ventricular tissue, *Sci. Rep.* **10**, 20632(2020).
- [36] S. F. Pravdin, T. V. Nezlobinsky, T. I. Epanchintsev, H. Dierckx, and A. V. Panfilov, Simulation of low-voltage cardioversion in a two-dimensional isotropic excitable medium using ionic cell models, in *Proceedings of the International Conference “Mathematical Analysis With Applications - In Honor of the 90th Birthday of Constantin Corduneanu” (2018)*, edited by S. Pinelas, A. Kim, and V. Vlasov, volume 318 of *Springer Proceedings in Mathematics & Statistics, Ekaterinburg* (Springer, Russia, 2020), pp. 273–288.
- [37] S. F. Pravdin, T. V. Nezlobinsky, and A. V. Panfilov, Inducing drift of spiral waves in 2D isotropic model of myocardium by means of an external stimulation, in *Proceedings of the 48th International Youth School-Conference “Modern Problems in Mathematics and its Applications”*, CEUR-WS, Yekaterinburg (IMM UB RAS, Russia, 2017), Vol. 1894, pp. 268–284.
- [38] S. F. Pravdin, T. V. Nezlobinsky, and A. V. Panfilov, Modelling of low-voltage cardioversion using 2D isotropic models of the cardiac tissue, in *Proceedings of the International Conference Days on Diffraction 2017* (IEEE, Saint Petersburg, 2017), pp. 276–281.
- [39] S. F. Pravdin, T. V. Nezlobinsky, A. V. Panfilov, and H. Dierckx, High-frequency pacing of scroll waves in a three-dimensional slab model of cardiac tissue, *Phys. Rev. E* **103**, 042420(2021).
- [40] D. Barkley, M. Kness, and L. S. Tuckerman, Spiral-wave dynamics in a simple model of excitable media: The transition from simple to compound rotation, *Phys. Rev. A* **42**, 2489 (1990).
- [41] A. Defauw, P. Dawyndt, and A. V. Panfilov, Initiation and dynamics of a spiral wave around an ionic heterogeneity in a model for human cardiac tissue, *Phys. Rev. E* **88**, 062703 (2013).
- [42] R. R. Aliev and A. V. Panfilov, A simple two-variable model of cardiac excitation, *Chaos, Solitons & Fractals* **7**, 293 (1996).
- [43] W.-J. Rappel, Intermittent trapping of spiral waves in a cardiac model, *Phys. Rev. E* **105**, 014404 (2022).
- [44] E. Rösslner and C. Kahlert, Winfree meandering in a 2-dimensional 2-variable excitable medium, *Z. Naturforsch. A* **34**, 565 (1979).
- [45] S. Alonso and A. V. Panfilov, Negative filament tension in the Luo–Rudy model of cardiac tissue, *Chaos* **17**, 015102 (2007).
- [46] S. Alonso and A. V. Panfilov, Negative Filament Tension at High Excitability in a Model of Cardiac Tissue, *Phys. Rev. Lett.* **100**, 218101 (2008).
- [47] F. Xie, Z. Qu, A. Garfinkel, and J. N. Weiss, Electrophysiological heterogeneity and stability of reentry in simulated cardiac tissue, *Am. J. Physiol.: Heart Circ. Physiol.* **280**, H535 (2001).